

Article

Spatiotemporal Variations of XCH₄ across China during 2003–2021 Based on Observations from Multiple Satellites

Jiayao Qin ^{1,2}, Xiuying Zhang ^{1,*}, Linjing Zhang ³, Miaomiao Cheng ⁴ and Xuehe Lu ⁵¹ International Institute for Earth System Science, Nanjing University, Nanjing 210023, China² Jiangsu Center for Collaborative Innovation in Geographical Information Resource Development and Application, Nanjing 210023, China³ College of Surveying and Geo-Informatics, North China University of Water Resources and Electric Power, Zhengzhou 450046, China⁴ State Key Laboratory of Environmental Criteria and Risk Assessment, Chinese Research Academy of Environmental Science, Beijing 100012, China⁵ School of Geography Science and Geomatics Engineering, Suzhou University of Science and Technology, Suzhou 215009, China

* Correspondence: zhangxy@nju.edu.cn

Abstract: Atmospheric methane (CH₄) is an important greenhouse gas that can reflect variations of CH₄ emissions and sinks. This study aimed to detect spatial and temporal variations of atmospheric CH₄ concentrations in China during 2003–2021 based on CH₄ column-averaged dry-air mole fraction (XCH₄) products from three satellites, namely, Scanning Imaging Absorption Spectrometer for Atmospheric Chartography (SCIAMACHY), Greenhouse Gases Observing Satellite (GOSAT), and Copernicus Sentinel-5 Precursor (S5P). The results revealed that XCH₄ observed from three satellites showed high agreement in spatiotemporal variations and demonstrated good consistency with ground station measurements. The correlation coefficients (*r*) between the three satellites were 0.72 and 0.73, and the correlation coefficients for the ground stations were 0.79, 0.66, 0.03, 0.21, 0.70, and 0.80. The spatial distribution of XCH₄ in China was generally high in the east and low in the west and close to that of CH₄ emissions, indicating that CH₄ emission sources dominated the spatial variations of atmospheric XCH₄. From 2003 to 2006, XCH₄ remained stable with an annual growth rate of 0.51 ppb·yr⁻¹ and then abruptly increased with an overall growth rate of 6.96 ppb·yr⁻¹. There were obvious seasonal changes in XCH₄, with peaks in autumn and summer and nadir in winter and spring. These seasonal variations of XCH₄ were related to CH₄ emissions from rice planting. Rice cultivation areas generally had high XCH₄ concentrations, and the growth cycle of rice plants significantly contributed to seasonal variations of XCH₄ in the main rice planting areas. These results provide scientific data that could encourage decision-makers to enact policies and processes to reduce methane emissions.

Keywords: methane; SCIAMACHY; GOSAT; Sentinel-5P; China

Citation: Qin, J.; Zhang, X.; Zhang, L.; Cheng, M.; Lu, X. Spatiotemporal Variations of XCH₄ across China during 2003–2021 Based on Observations from Multiple Satellites. *Atmosphere* **2022**, *13*, 1362. <https://doi.org/10.3390/atmos13091362>

Academic Editor: Dmitry Belikov

Received: 23 July 2022

Accepted: 23 August 2022

Published: 25 August 2022

Publisher's Note: MDPI stays neutral with regard to jurisdictional claims in published maps and institutional affiliations.



Copyright: © 2022 by the authors. Licensee MDPI, Basel, Switzerland. This article is an open access article distributed under the terms and conditions of the Creative Commons Attribution (CC BY) license (<https://creativecommons.org/licenses/by/4.0/>).

1. Introduction

Methane (CH₄) is an important greenhouse gas, second only to carbon dioxide [1]. The radiative forcing of CH₄ is more than 80 times that of carbon dioxide. From 1750 to 2020, the increasing ratio of CH₄ concentrations was more than three times that of CO₂ [2,3]. This rapid increase in atmospheric CH₄ deserves much attention; however, spatial and temporal variations of methane emissions have not been well understood [4]. As China is one of the countries with the largest carbon emissions, it is critical to understand temporal and spatial variations of atmospheric CH₄ concentrations to help formulate effective emission reduction strategies.

Several techniques have been developed to measure atmospheric CH₄ concentrations, including ground-based, aircraft, and satellite monitoring. Among these methods,

satellites can observe temporal and spatial variations of CH₄ concentrations on a regional or global scale [5]. Several sensors can provide CH₄ concentrations, such as the Atmospheric Chemistry Experiment Fourier Transform Spectrometer (ACE-FTS), Atmospheric Infrared Sounder (AIRS), Infrared Atmospheric Sounding Interferometer (IASI), Michelson Interferometer for Passive Atmospheric Sounding (MIPAS), Scanning Imaging Absorption Spectrometer for Atmospheric Chartography (SCIAMACHY), Greenhouse Gases Observing Satellite (GOSAT), Tropospheric Emissions Spectrometer (TES), and Tropospheric Monitoring Instrument (TROPOMI) mounted on Copernicus Sentinel-5 Precursor (S5P). Since 2002, these satellites have provided gridded daily or monthly data products on CH₄ concentrations in the atmosphere on a global capacity. CH₄ column-averaged dry air mole fractions (XCH₄) is defined as the total column amount of CH₄ divided by the total column amount of dry air, and it is often used to study variations of atmospheric CH₄.

These satellite observations have been used to study spatial and temporal distribution of CH₄ concentrations in the atmosphere and their driving forces on a regional scale. Based on SCIAMACHY, Zhang analyzed the spatial distribution of XCH₄ in China during 2003–2005 [6], Kavitha studied the trends in XCH₄ over the Indian region during 2003–2009 [7], and Frankenberg reported trends and variability of XCH₄ globally during 2003–2009. Based on GOSAT, Qin preliminarily assessed XCH₄ variations in China during 2010–2012 [8], Kivimäki analyzed the average XCH₄ between latitudes 44.43° S and 53.13° N during 2009–2017 [9], and Islam detected XCH₄ trends in Western Canada for the period 2009–2019 [10]. Zhang studied XCH₄ spatial distribution in China using S5P during 2018–2021 [11]. Most of these studies used observations from one satellite to study the long-term variations of CH₄ in China over no more than 10 years due to the limited life cycle of one single satellite.

Fortunately, although these satellites carried different instruments to observe CH₄ in the atmosphere, the CH₄ concentrations from different satellites presented relative consistency. For example, Zou found that the correlation coefficients of CH₄ columns from AIRS and GOSAT were more than 0.8 and that the difference was larger in high-latitude regions than in lower-latitude regions [12]. Hu presented a comparison of XCH₄ products from S5P and GOSAT that showed excellent consistency [13]. Zhang found that atmospheric CH₄ from AIRS, SCIAMACHY, and GOSAT were in good agreement with those from ground-based measurements [14]. These studies highlight the potential of studying long-term variations based on serious observations from satellites.

In the present study, we aimed to obtain an overall insight on spatiotemporal trends of CH₄ based on monthly XCH₄ products from multiple satellite observations, namely, SCIAMACHY, GOSAT, and S5P. The rest of the paper is structured as follows. Section 2 introduces data sources and methods, Section 3 demonstrates the accuracy and consistency of satellite data on XCH₄ and analyzes spatiotemporal variations of XCH₄ concentrations in China. The effects of rice planting on the seasonal cycle of XCH₄ are then evaluated, and the analysis is summarized in Section 4.

2. Materials and Methods

2.1. Materials

2.1.1. Satellite-Observed Atmospheric XCH₄

SCIAMACHY on board ENVISAT (Environmental Satellite) was launched in March 2002 [15]. The spectral information in 2360–2385 nm at spectral resolutions of 0.2 nm was used to retrieve data on CH₄. XCH₄ was inverted from the proxy algorithm by applying WFM-DOAS to a small spectral fitting window in SCIAMACHY. This method assumes that the scattering effect is offset in the CH₄ to CO₂ column ratio and that prior estimation of the CO₂ column is accurate enough to reliably recalculate the CH₄ column according to this ratio [16]. The SCIAMACHY monthly XCH₄ data (from January 2003 to December 2011) used in this study were provided by Bremen University in Germany and were retrieved by the WFM-DOAS algorithm [15,17–19].

GOSAT was launched on 23 January 2009 with the aim of estimating global distributions and temporal variations of greenhouse gas emissions. It was equipped with TIR and NIR Sensor for Carbon Observation Fourier Transform Spectrometer (TANSO-FTS) and Cloud and Aerosol Image (CAI). The TANSO-FTS measures greenhouse gases, while the CAI detects clouds and aerosols [20–22]. This study used XCH₄ data from the bias-corrected FTS level 2 CH₄ products (v02.95) from January 2010 to December 2021.

S5P was the first Copernicus mission and provided data on atmospheric CH₄ concentration that have high sensitivity to the lower atmosphere and high spatiotemporal resolution to facilitate understanding of methane sources and sinks. It was launched on 13 October 2017 carrying a single instrument, TROPOMI. For this study, we used S5P RPRO (L2) CH₄ products from January 2019 to August 2019 with a spatial resolution of 7×7 km² and products from August 2019 to December 2021 with a spatial resolution of 5.5×7 km². These were stored in netCDF format, and pixels with qa_value < 0.8 were filtered to ensure data quality.

2.1.2. Ground Observations of CH₄ Concentrations from WDCGG

The ground observations of CH₄ from the World Data Centre for Greenhouse Gases (WDCGG) were used to evaluate the satellite observations. WDCGG is one of seven Global Atmosphere Watch Program (GAW) world data centers responsible for archiving greenhouse gas monitoring. The estimated precision of measurements of CH₄ concentrations is $\pm 0.2\%$ [23]. We obtained monthly measurements of CH₄ concentrations from six ground stations located in and close to China. Lulin (LLN), Shangdianzi (SDZ), and Waliguan (WLG) are located in China [24], while Anmyeon do (Amy), Pha Din (PDI), and Ulaan UUL (UUM) are located in areas near China. Monthly data from 2003 to 2021 was collected, and CH₄ concentrations that deviated by two times the standard deviation were excluded to ensure data quality. More specific information about the six stations is shown in Table A1.

2.1.3. CH₄ Emissions from EDGAR

The gridded CH₄ emissions database in China was from the Emissions Database for Global Atmospheric Research (EDGAR), which is a widely used inventory for anthropogenic emissions of greenhouse gases on Earth. EDGAR provides CH₄ emission estimation from sector-specific grid maps at $0.1^\circ \times 0.1^\circ$ resolution with yearly, monthly, and hourly data using the IPCC methodology. This study collected data on yearly CH₄ total emissions from all sectors and monthly sector-specific grid maps for 2003–2018.

2.1.4. Enhanced Vegetation Index from MODIS

As an optimized vegetation index, enhanced vegetation index (EVI) is less influenced by the atmosphere or underlying surface, has improved sensitivity in high biomass areas, and can be used to estimate the gross primary production of paddy rice [25]. The EVI in China was from the National Aeronautics and Space Administration. The dataset used a MODIS-specific synthesis method to remove low-quality pixels to ensure product quality, with temporal resolutions of 16 days and one month and spatial resolutions of 250 m, 500 m, 1 km, and 0.05° . In this study, we used monthly MODIS-based EVI from 2003 to 2021 with spatial resolution of a $0.05^\circ \times 0.05^\circ$ grid.

2.1.5. Rice-Harvested Area from EARTHSTAT

The gridded dataset of rice-harvested area was provided by University of Minnesota and University of British Columbia. This dataset was created by collecting census statistics at the national, state, and county levels. The database describes the average fractional proportion of rice paddy crop areas at a spatial resolution of $10 \text{ km} \times 10 \text{ km}$ and could represent the complete and detailed source of spatial agricultural systems in existence.

2.2. Methods

2.2.1. Inverse Distance Weighted Interpolation Method

The inverse distance weighted (IDW) interpolation method accounts for the reciprocal relationship between distance and weight, which can interpolate in an exact and smooth way to estimate the value of an unobserved point [26]. The IDW function is as follows:

$$V_e = \sum_{i=1}^n w_i v_i \tag{1}$$

where V_e is the point (x_e, y_e) to be evaluated, v_i ($i = 1, 2, \dots, n$) is the observation point (x_i, y_i) involved in interpolation around (x_e, y_e) , and w_i is the weight coefficient that can be calculated as follows:

$$W_i = \frac{d_{ej}^{-p}}{\sum_{i=1}^n d_{ej}^{-p}} \tag{2}$$

where n is the number of points involved in interpolation, d_{ej} is the distance between (x_e, y_e) and (x_i, y_i) , and $p = 1$ or 2 and represents the function of reciprocal or reciprocal squares of distance, respectively. The IDW method was utilized for the area without a value to help generate the monthly average XCH₄ grid datasets for SCIAMACHY, GOSAT, and S5P with a grid resolution of $0.5^\circ \times 0.5^\circ$.

2.2.2. A Linear Sinusoidal Trend Model with a Seasonal Component

A linear sinusoidal trend model has been widely used to detect long-term trends and seasonal variations of atmospheric components. This model was used to simulate the trends of atmospheric SO₂, CH₄, and NO₂ in China [27–29]. The long-time trends of XCH₄ concentrations over China from January 2003 to December 2021 were simulated using a linear sinusoidal trend model.

The model formula is as follows:

$$Y_i = A + BX_i + C \sin(DX_i + E) + M_i \tag{3}$$

where Y_i represents the monthly XCH₄ concentrations (ppb) at month i ; X_i is the number of months after January 2003; M_i is the residual; and $A, B, C, D,$ and E are the function parameters.

2.2.3. Mann–Kendall Test and Theil–Sen Estimator

The Mann–Kendall (MK) test is a nonparametric time-series trend test method that does not need the measured values to obey the normal distribution and is not affected by missing values and outliers [30]. It is suitable for trend significance test of long-time series data. Based on the time-series variables (x_1, x_2, \dots, x_n) , the statistic variable S is calculated as follows:

$$S = \sum_{i=1}^{n-1} \sum_{j=i+1}^n \text{sgn}(x_j - x_i) \tag{4}$$

with the sample size $n > 10$, the standard normal test statistic Z_{MK} is calculated using the following equation:

$$Z_{MK} = \begin{cases} \frac{S}{\sqrt{\text{Var}(S)}}, & (S > 0) \\ 0, & (S = 0) \\ \frac{S+1}{\sqrt{\text{Var}(S)}}, & (S < 0) \end{cases} \tag{5}$$

where $\text{Var}(S)$ is the variance and is calculated using the following equation:

$$\text{Var}(S) = \frac{n(n-1)(2n+5) - \sum_{p=1}^g t_p(t_p-1)(2t_p+5)}{18} \tag{6}$$

where p is the number of tied (same data observed) groups, and t_p denotes the number of ties (same data observed) of extent p . A positive value of Z_{MK} indicates an upward trend,

and a negative value of Z_{MK} indicates a downward trend. The absolute value of Z_{MK} is greater than or equal to 1.28, 1.64, and 2.32, indicating that the upward and downward trend of this sequence has passed the significance test of 90%, 95%, and 99% reliability, respectively [31].

The Theil–Sen estimator is a robust nonparametric statistical trend calculation method with high computational efficiency and insensitive to measurement errors and outlier data [32]. Based on the time-series variables (x_1, x_2, \dots, x_n) , the Theil–Sen slope β can be calculated as shown in Equation (7):

$$\beta = \text{Median} \left(\frac{x_j - x_i}{j - i} \right) \forall j > i \tag{7}$$

The nonparametric Mann–Kendall and Theil–Sen slopes have been widely used in the fields of environment, hydrology, meteorology, and climatology by various authors [33–35].

3. Results and Discussion

3.1. Validation of Satellite XCH₄ Accuracy and Consistency

The observed CH₄ concentrations at six stations from WDCGG were used to test whether the XCH₄ data from satellite observations could reflect temporal variations and spatial distributions of CH₄ in the atmosphere (see Figure 1 and Table 1). The scatter plots showed there was good consistency between satellite-observed XCH₄ concentrations and ground-observed CH₄ concentrations except for PDI and SDZ. These results showed that satellite-observed XCH₄ could indicate spatiotemporal variations of atmospheric CH₄ at the four sites. The low correlation coefficient (r) at PDI and SDZ might be because there were only a few valid ground observations and we synthesized the monthly mean CH₄ concentrations from satellite observation and ground observation to analyze their relevance. SDZ is located in Beijing, one of the biggest cities in China, where human activities and industrial production have more influence on ground-level CH₄ concentrations than atmospheric CH₄ [36]. PDI is in Vietnam, where CH₄ might be affected by tropical long-distance atmospheric transmission [37].

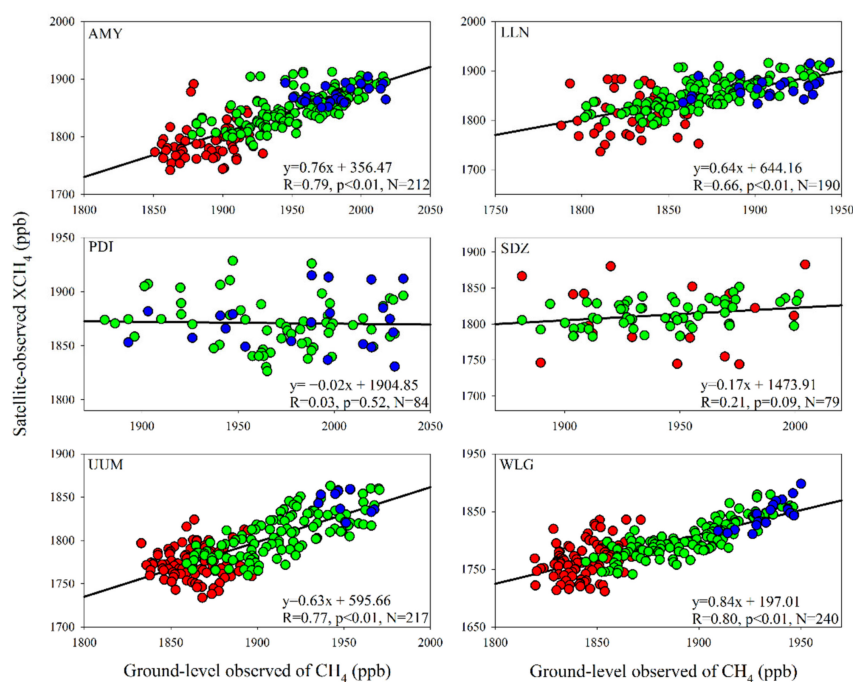


Figure 1. Scatter plots of satellite-observed XCH₄ concentrations and ground-level observations of CH₄ concentrations; red: SCIAMACHY, green: GOSAT, blue: S5P.

Table 1. The correlation between satellite-observed XCH₄ concentrations and ground measurement of CH₄ concentrations.

Sites	Satellites	Regression	R	p	RMSE	N
AMY	SCIAMACHY	$y = 0.39x + 1047.77$	0.27	0.04	52.21	61
	GOSAT	$y = 0.65x + 584.04$	0.69	<0.01	77.24	128
	S5P	$y = 0.27x + 1331.06$	0.37	0.08	34.32	23
LLN	SCIAMACHY	$y = 0.07x + 1686.86$	0.03	0.84	19.77	43
	GOSAT	$y = 0.678x + 583.08$	0.75	<0.01	21.64	125
	S5P	$y = 0.35x + 1205.98$	0.40	0.07	14.59	22
PDI	SCIAMACHY					
	GOSAT	$y = -0.06x + 1986.99$	0.10	0.44	56.39	63
	S5P	$y = 0.08x + 1721.49$	0.13	0.57	35.84	21
SDZ	SCIAMACHY	$y = 0.01x + 1794.79$	0.01	0.98	41.58	20
	GOSAT	$y = 0.26x + 1312.77$	0.43	<0.01	65.06	59
	S5P					
UUM	SCIAMACHY	$y = 0.04x + 1692.94$	0.04	0.73	57.43	92
	GOSAT	$y = 0.66x + 552.70$	0.73	<0.01	75.49	116
	S5P	$y = -0.47x + 2758.41$	0.40	0.28	20.98	9
WLG	SCIAMACHY	$y = 0.98x - 39.40$	0.41	<0.01	52.72	98
	GOSAT	$y = 1.06x - 203.27$	0.84	<0.01	68.03	126
	S5P	$y = 1.72x - 1484.19$	0.81	<0.01	26.07	20

Figure 1 shows that the observed CH₄ concentrations were obviously higher than the satellite measurements of XCH₄ concentrations. This is because ground-level CH₄ concentrations are more influenced by emissions than those in the atmosphere as CH₄ can be transported in the direction of atmospheric movement after being emitted into the atmosphere. Its concentrations show decreased gradient in the vertical directions, with the highest CH₄ concentrations often occurring at the surface [38]. Table 1 shows that CH₄ from ground measurements showed more consistency with XCH₄ from GOSAT and S5P than from SCIAMACHY. The lowest correlation coefficient between GOSAT and ground measurements was 0.69, the highest correlation coefficient between SCIAMACHY and ground measurements was 0.41, and the correlation between S5P and ground measurements were between the two satellites.

It is important to note that data consistency between satellites has been proven in previous studies, so the specific value of the observation difference was not the main research objective of this study. However, considering that the systematic error between different satellites in China has not been studied and that this is important for the accuracy of spatiotemporal distribution through satellites with different time coverage, the uncertainty caused still needs to be discussed. The uncertainty of satellite observation is mainly due to the observation modes, CH₄-retrieved algorithms, the instruments themselves, and height sensitivities [39–41]. The specific parameters of the three satellites are shown in Table 2. The reliability of the satellite itself should be determined before considering the differences between satellites. The accuracy of SCIAMACHY was verified by ground-based FTS measurements [42,43] and model simulation [44], with the overall error being below 5%. The relative deviation between GOSAT and China's Hefei Station was about 0.34% [45], while GOSAT XCH₄ data was consistent with aircraft-based measurements with a standard deviation of 14.9 ppb [46]. For S5P, the data was compared with COCCON and TCCON measurements, and the systematic difference was in the range of 3–6% on average [47–49]. These results show the reliability of satellite measurements, but the error between different satellites requires further comparison of the satellite products. Hu showed a comparison between GOSAT and S5P on the global scale and found an excellent agreement with a mean difference of 13.6 ppb [13]. Monteil performed a comparison between SCIAMACHY and GOSAT and found a remarkable agreement [50]. This suggests that the quality of satellite XCH₄ data is comparable on a global scale. However, the consistency of satellite XCH₄ products in China is still uncertain.

Table 2. Main parameters of three satellites.

Satellite	SCIAMACHY	GOSAT	Sentine-5P
Launch time	Mar, 2002	Jan, 2009	Oct, 2017
Orbit(km)	772	666	824
Accuracy(ppb)	-	37	5.6
Spectral coverage(um)	0.21–2.38	0.76–14.33	0.27–0.775 2.305–2.385
CH ₄ band(um)	2.36–2.38	1.56–1.72 5.56–14.33	0.25–1.0
Swath(km)	960	640	2600
Spatial resolution(km)	32 × 60	10.5	7 × 5.5
Viewing Model	limn sounders nadir looking occultation mode	nadir lloking	nadir looking
CH ₄ algorithm	WFM-DOAS	Optimization algorithm	WFM-DOAS

To analyze the deviations of XCH₄ products from different satellites over China, we compared their observation results during the overlap time in Figure 2. The results showed that, on the pixel scale, the bias between SCIAMACHY and GOSAT ranged from −55 to 65 ppb with an average of 2.36 ppb, and the bias between S5P and GOSAT ranged from −45 to 38 ppb with an average of 1.90 ppb. At a pixel scale, the scatter plot showed that the mean XCH₄ concentrations of SCIAMACHY and GOSAT were 1792.34 and 1794.94 ppb with a correlation coefficient of 0.73. The mean XCH₄ concentrations of S5P and GOSAT were 1874.39 and 1873.58 ppb, respectively, and the correlation coefficient was 0.72. These results indicated that the overall observations of different satellites in China were highly consistent.

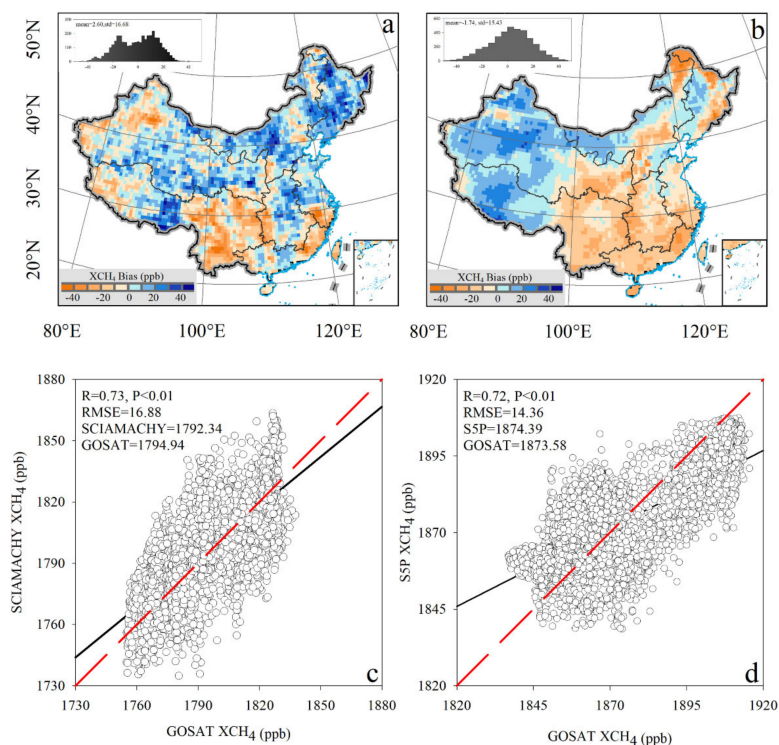


Figure 2. Comparison of XCH₄ concentrations from different satellites. (a) The XCH₄ bias calculated by subtracting GOSAT data from SCIAMACHY data during the overlap time (January 2010 to December

2011); (b) the XCH₄ bias calculated by subtracting GOSAT data from S5P data during the overlap time (January 2019 to December 2021); (c) scatter plots of the monthly averaged XCH₄ concentrations between GOSAT and SCIAMACHY during the overlap time (January 2010 to December 2011); and (d) scatter plots of the monthly averaged XCH₄ concentrations between GOSAT and S5P during the overlap time (January 2019 to December 2021).

3.2. Spatial Distribution Patterns of Atmospheric XCH₄ across China

To analyze the spatial distribution patterns of XCH₄ across China, the spatial distribution of multi-year-averaged XCH₄ concentrations from three satellites and the multi-year-averaged CH₄ emissions from EDGAR are illustrated in Figure 3. The range, average, and standard deviation of XCH₄ concentrations from SCIAMACHY, GOSAT, and S5P were 1728 to 1835, 1777, and 18.52 ppb; 1784 to 1858, 1818, and 21.01 ppb; and 1819 to 1924, 1873, and 17.26 ppb, respectively. The spatial distributions of XCH₄ from the three satellites were close, but SCIAMACHY and S5P provided more detailed information than GOSAT. The XCH₄ concentrations showed greatly spatial variation in different regions of China and presented spatial cluster in different regions. Overall, there were low XCH₄ concentrations in western China and high concentrations in eastern China (109–122° E, 20–41° N). Because CH₄ is a long-lived gas that can exist in the atmosphere for 12.5 years, the spatial variations of atmospheric CH₄ concentrations might reflect the accumulation of CH₄ emissions and transportations.

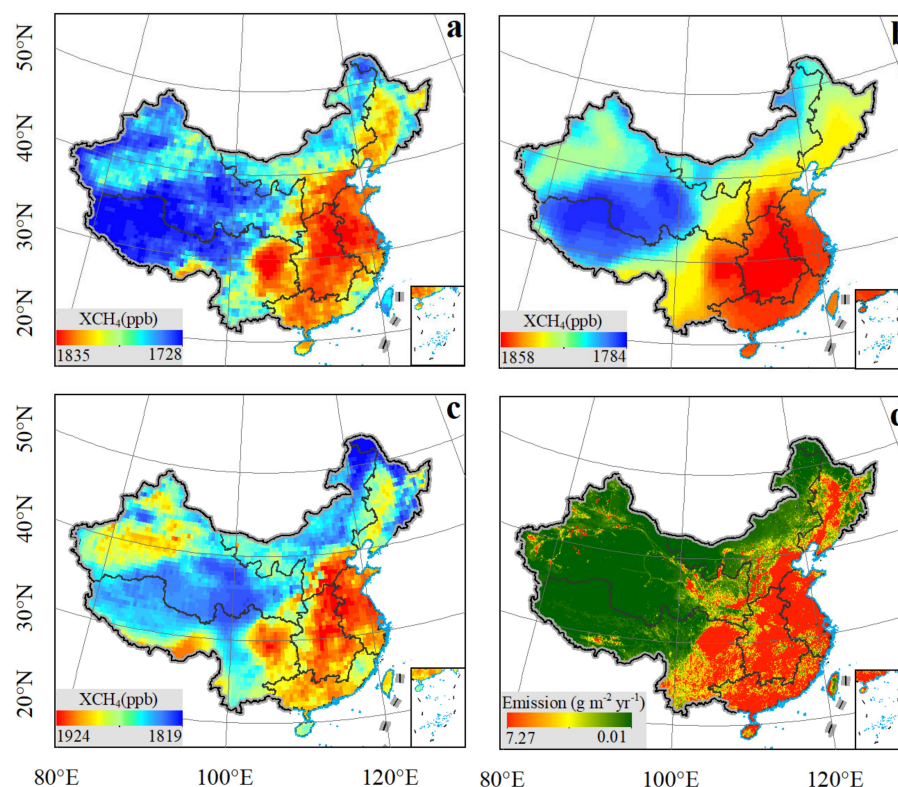


Figure 3. Spatial distribution of multi-year averages of atmospheric XCH₄ and CH₄ emissions over all of China. (a) XCH₄ concentrations from SCIAMACHY (January 2003 to December 2010); (b) XCH₄ concentrations from GOSAT (January 2011 to December 2018); (c) XCH₄ concentrations from S5P (January 2019 to December 2021); and (d) CH₄ emission from EDGAR (2003 to 2018).

The regions with high XCH₄ concentrations were mainly distributed in Central China, East China, Sichuan Basin in Southwest China, and Beijing Tianjin Hebei region in North China, where the XCH₄ concentrations were approximately 29 ppb higher than China's average. The secondary high areas were found in South China, some regions of Northeast

China, some regions of Tibet bordering India, and the Tarim Basin. The XCH₄ concentrations in these areas were approximately 9 ppb higher than China's average. The lowest XCH₄ were in the Qinghai Tibet Plateau and Inner Mongolia Plateau, where the concentrations were approximately 17 ppb lower than China's average.

In terms of EDGAR CH₄ emission spatial distribution in Figure 3d, the spatial distribution pattern of satellite-observed XCH₄ was highly consistent with CH₄ emission, indicating XCH₄ observed by satellite could reflect the spatial distribution of methane emissions. Regions with high XCH₄ concentrations were mostly distributed near areas of high population density, large energy consumption, developed industrial activities, and large rice-growing areas.

To further analyze the contribution of CH₄ emission from different sectors to the spatial distribution of high XCH₄ concentrations, we obtained the sector-specific CH₄ emission from EDGAR. The XCH₄ sources were divided into six categories according to the IPCC code: energy manufacturing, coal/oil/gas production, industrial process, agricultural animal (including enteric fermentation and manure management), agricultural soil (including rice cultivation and field burning of agricultural residues), and waste disposal (See Figure A1). China emitted about 80,000 Gg·yr⁻¹, of which about 50% came from coal and oil exploitation, 30% from agricultural emissions, 15% from waste treatment, and others were mainly from industrial emissions and energy consumption.

Coal and oil exploitation emissions were at a very low level in most parts of China and mainly distributed in Shanxi, northwest Xinjiang, and other coal or oil fields, presenting highly spatial clusters. For agricultural emissions, rice cultivation emissions were mainly distributed in Sichuan Basin, Northeast China, and some regions of Northeast China, while enteric fermentation and manure management emissions were mainly distributed in North China. Waste disposal emissions areas were mainly distributed in densely populated areas, such as North China, Sichuan, Jiangsu, and Guangdong. This shows that CH₄ emissions from different sources present different spatial clusters and further explains the spatial variations of XCH₄ concentrations across China. We also computed the share of individual sectors in methane emissions (Figure A2). The main emission sources differed from the north to the south, with industrial-related emissions dominant in the north and agricultural emissions dominant in the south. Oil and coal mining in the northern region accounted for the main part of methane emissions, especially in Heilongjiang, Shanxi, Liaoning, Hebei, and Tibet. The rice emissions dominated anthropogenic emission in Southeast China, such as Zhejiang, Jiangsu, Jiangxi, Hunan, and other major rice planting areas.

For the Sichuan Basin and Southeast China (109–122° E, 20–34° N), including Jiangsu, Anhui, Hubei, Jiangxi, Fujian, Zhejiang, Guangdong, and Yunnan, high value of XCH₄ concentrations in these areas were mainly caused by emissions from rice planting. These areas with high agricultural soil CH₄ emissions, with total emissions reaching 10,732 Gg·yr⁻¹, accounted for about 78% of China's total agricultural soil emissions. These areas and the surrounding environment have appropriate temperature, sufficient sunlight and water, and rich organic nutrients, which provide good environmental conditions for the growth of rice and breeding of methanogens.

The Beijing Tianjin Hebei region has a large population, heavy industry, and serious waste pollution. Emissions in this region was mainly dominated by animal husbandry and waste disposal, with emissions from these sources reaching 2087 and 2475 Gg·yr⁻¹, accounting for 23% and 19% of China's total emissions, respectively. Energy manufacturing was also relatively high in this area, but the emission level was low. Shanxi is the major energy-producing area in China, and the CH₄ emissions caused by the exploitation of coal accounted for more than half of China's total coal/oil/gas production emission. For the high XCH₄ concentrations in Northeast China, its spatial distribution was highly consistent with agricultural emissions and waste management. Northeast China has been a major rice planting area with many industrial bases producing substantial CH₄ emissions. In the Tarim Basin, the high XCH₄ concentrations observed might be due to the Tarim, Tahe,

and Baolang oilfields, which are distributed in the Tarim Basin, with the coal/oil/gas production emission reaching $1772 \text{ Gg}\cdot\text{yr}^{-1}$.

3.3. Temporal Variation of Atmospheric XCH_4 across China

The linear sinusoidal trend-fitting model was employed to simulate temporal variations of XCH_4 concentrations in China during 2003–2021, and a high R^2 (0.93 , $p < 0.01$) was obtained (Figure 4). In January 2003, the simulated XCH_4 concentration was about 1747 ppb , which increased $0.58 \text{ ppb}\cdot\text{month}^{-1}$ to December 2021. The monthly XCH_4 concentration amplitude in the annual cycle was 14.15 ppb , indicating XCH_4 concentrations had obvious seasonal variations over a one-year cycle. Comparing the fitting coefficients among satellite-observed XCH_4 concentrations over China and ground measurement from WDCGG stations (Table 3), the amplitude of seasonal variations and the growth trend were quite different in each site. Overall, the XCH_4 concentrations increased from 2003 to 2021 with obvious seasonal variation cycles each year. Therefore, it is necessary to describe temporal characteristics from long-term annual trends and seasonal variations.

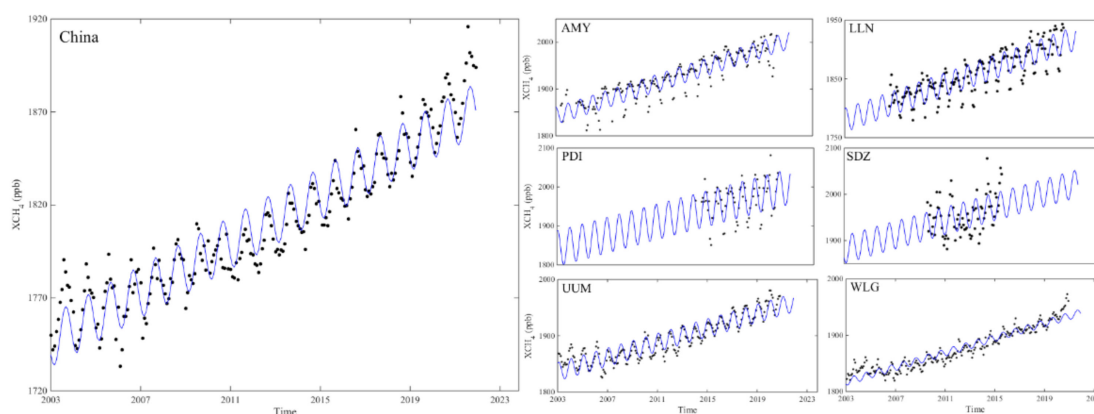


Figure 4. Linear sinusoidal trend model fitting results of the monthly mean XCH_4 concentrations over China from January 2003 to December 2021.

Table 3. Comparison of the linear sinusoidal trend mode parameters for China and the ground stations.

Sites	A	B	C	D	R^2	RMSE
China	1747	0.55	−14.15	1.53	0.93	10.08
AMY	1843	0.71	18.95	1.63	0.87	16.98
LLN	1780	0.61	20.71	1.15	0.80	16.68
PDI	1842	0.70	46.96	1.30	0.61	29.54
SDZ	1881	0.63	30.66	3.75	0.41	32.54
UUM	1836	0.54	16.75	1.07	0.91	11.30
WLG	1817	0.54	6.54	3.83	0.91	10.96

3.3.1. Long-Term Annual Trends of XCH_4 Concentrations across China

Before the satellite observations, CH_4 concentrations were assessed through ground measurement, aircraft sampling, and polar ice core samples. The data revealed a significant increase in CH_4 levels since the 1850s. The global CH_4 growth rate showed a decreasing trend from 1980 to 2000, then stabilized from 1999 to 2006, and has been increasing since 2007 [51–56]. It should be noted that measurements from sparse distribution can reflect the global average trend, and analyzing the growth of spatial distribution requires continuous satellite observations.

To analyze the annual trends of XCH_4 concentration variations over China during 2003–2021 on the grid, we used a nonparametric Mann–Kendall test to examine the monotonic trends of XCH_4 concentrations and then computed the Theil–Sen slope over grids that passed the Mann–Kendall test to obtain the annual growth rate map of XCH_4 concentrations (Figure 5). Because all pixels over China had a significant XCH_4 concentration growth

trend ($p < 0.1$), a nonparametric Theil–Sen slope estimator was used to compute the slope of XCH₄ concentrations, and the growth rate of XCH₄ ranged from 4.07 to 9.77 ppb·yr⁻¹. The slope of XCH₄ concentrations showed obvious latitudinal gradient distribution, presenting high slope in the south and low slope in the north (Figure 5c). This may be due to the obvious growth of human activities in the low latitude region, which has been the main population migration area in the last two decades. Regions with high growth rates were mainly distributed in Southeast China, the junction of Hubei, Sichuan, and Shanxi, where there have been large population activity and oil and gas exploitation. The Yunnan border, Tibet border, and Tarim Basin also had relatively high growth, which was perhaps caused by long-distance air mass transmission and the increasing rate of CH₄ concentrations in the mid-upper troposphere [27,57].

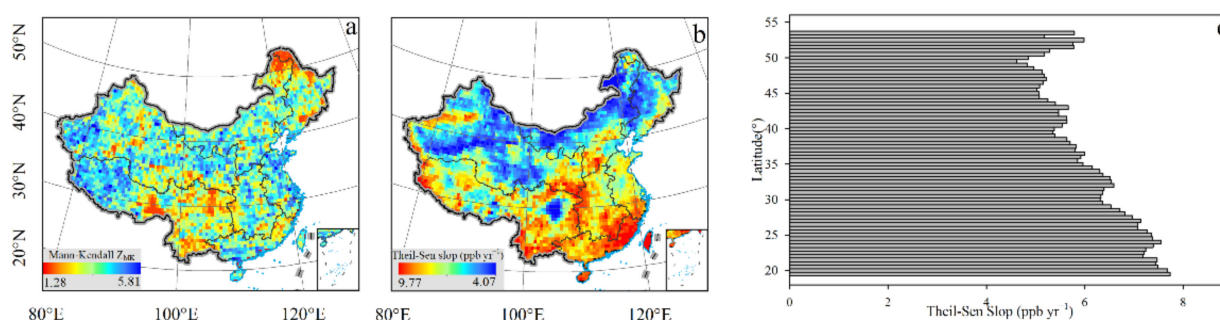


Figure 5. Spatial distribution of the annual rate of increase in XCH₄ concentrations from 2003 to 2021. (a) Mann–Kendall trend test map for XCH₄ concentrations over China; (b) Theil–Sen slope trend map for XCH₄ concentrations over China; (c) Theil–Sen slope distribution at different latitudes, varying by 0.5°.

The spatial distribution of the growth of different types of CH₄ emissions in China was calculated to analyze the driving factors of XCH₄ concentrations (Figure A3). Unlike XCH₄, the growth of CH₄ emissions was not obvious in some regions and some sources and even showed a downward trend. Among these different CH₄ emission sources, agricultural soil and coal/oil/gas production had the most significant upward trend. Studies have shown that global CH₄ emission from coal mining increased about 17 Tg·yr⁻¹, with dominant contribution from China [58]. With the improvement of agricultural production technology, management of fertilization measures, and rice expansion and intensification, CH₄ emissions from rice have inevitably increased [59]. China’s rapid productivity has contributed to an increase in energy exploitation, consumption, and industrial production. In Shanxi, Shaanxi, and other major coal resource development provinces as well as in North China, where heavy industry dominates, increased energy consumption and anthropogenic activities have led to increased CH₄ emissions.

Further analysis of the long-term annual trends of XCH₄ concentrations over China was conducted on a regional scale. China was divided into seven regions based on the geographic division rules, and the annual average XCH₄ concentrations in each region are shown in Figure 6. The bias of XCH₄ concentrations between different regions was complex for SCIAMACHY and S5P observations but stable for GOSAT. This may be because coverage from GOSAT was relatively low and the spatial details were erased during inverse distance interpolation. XCH₄ concentrations were higher in CC, SC, and EC compared to NE, NC, SW, and NW. XCH₄ concentrations in SW was lower than NE and NC before 2014, exceeded NC after 2015, then exceeded NE after 2018. The XCH₄ concentrations in SC, SW, and CC all decreased in 2006. CC rose in 2007 and 2008, decreased in 2009, and has been rising again since then. SC increased until 2015, decreased in 2016, and has been increasing again, while SW has presented an increasing trend since 2006. Previous studies have shown that global atmospheric CH₄ remained stable in the early 2000s and increased again after 2006 [60]. Similar trends of XCH₄ were found in China, where XCH₄ concentrations in the seven regions remained stable during 2003–2006 and even slightly decreased (with

an average annual growth rate of $0.51 \text{ ppb}\cdot\text{yr}^{-1}$) but then increased after 2006 (with an average annual growth rate of $7.87 \text{ ppb}\cdot\text{yr}^{-1}$).

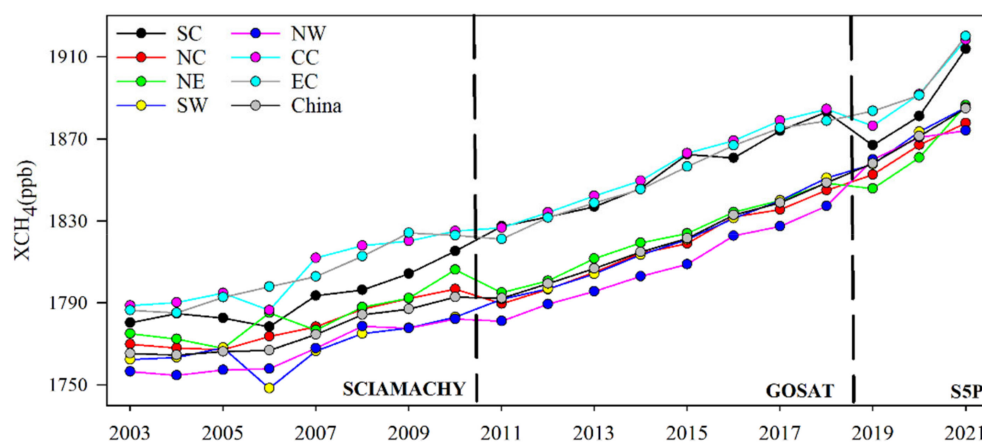


Figure 6. Annual averages of XCH_4 concentrations in the seven regions and China overall from 2003 to 2021.

3.3.2. Seasonal Cycle of XCH_4 Concentrations across China

From the three satellites, the average XCH_4 concentrations in China decreased from December to February, then increased, peaked in August, and decreased again. The peak XCH_4 concentrations occurred in summer (August), and the minimum value was in spring (February) (Figure 7). The seasonal cycle of XCH_4 concentrations is determined by the combined effects of CH_4 emission sources and sinks [2]. Atmospheric oxidation is the main CH_4 sink, and elimination from OH in the troposphere is the main mechanism of atmospheric CH_4 loss, accounting for about 85–90% [61]. As the concentrations of OH radicals are basically stable with little seasonal variation, the oxidation-cleaning effect of OH radicals have a weak impact on the seasonal variation of XCH_4 concentrations [62]. Meanwhile, the seasonal variation of CH_4 emission in rice fields, wetlands, and marshes is obvious. Temperature is a major factor in the anaerobic decomposition process and the release of methane by microorganisms in biological sources. Therefore, high temperatures and increase in microbial activity and quantity in summer may have contributed to the identified CH_4 emission peaks [63].

The monthly changes in six different categories of CH_4 emissions are shown in Figure A4. Among these emissions, agricultural soil had the most obvious seasonal changes, with emissions reaching the maximum in summer and the lowest in spring and winter. However, industrial emissions, energy consumption, and other emissions impacted by human activities were not associated with significant seasonal changes. Previous studies have shown that rice planting emissions is the key factor leading to maximum average CH_4 concentrations in summer [64,65]. Higher temperature and humidity provide good conditions for growth of rice paddies and increase the rate of root decay to provide abundant substrates for CH_4 production, while flooded rice paddies help biomass-related methanogens release CH_4 [66]. In winter, with drainage and drying of the fields, CH_4 emissions from paddy fields are greatly reduced. Meanwhile, CH_4 emissions from natural sources, including wetlands, frozen soil, biomass combustion, and plants, are also at low levels in winter. Individually and combined, these environmental and human factors could affect seasonal variations of XCH_4 concentrations, leading to the pattern of high CH_4 concentrations in warm season and low CH_4 concentrations in cold season.

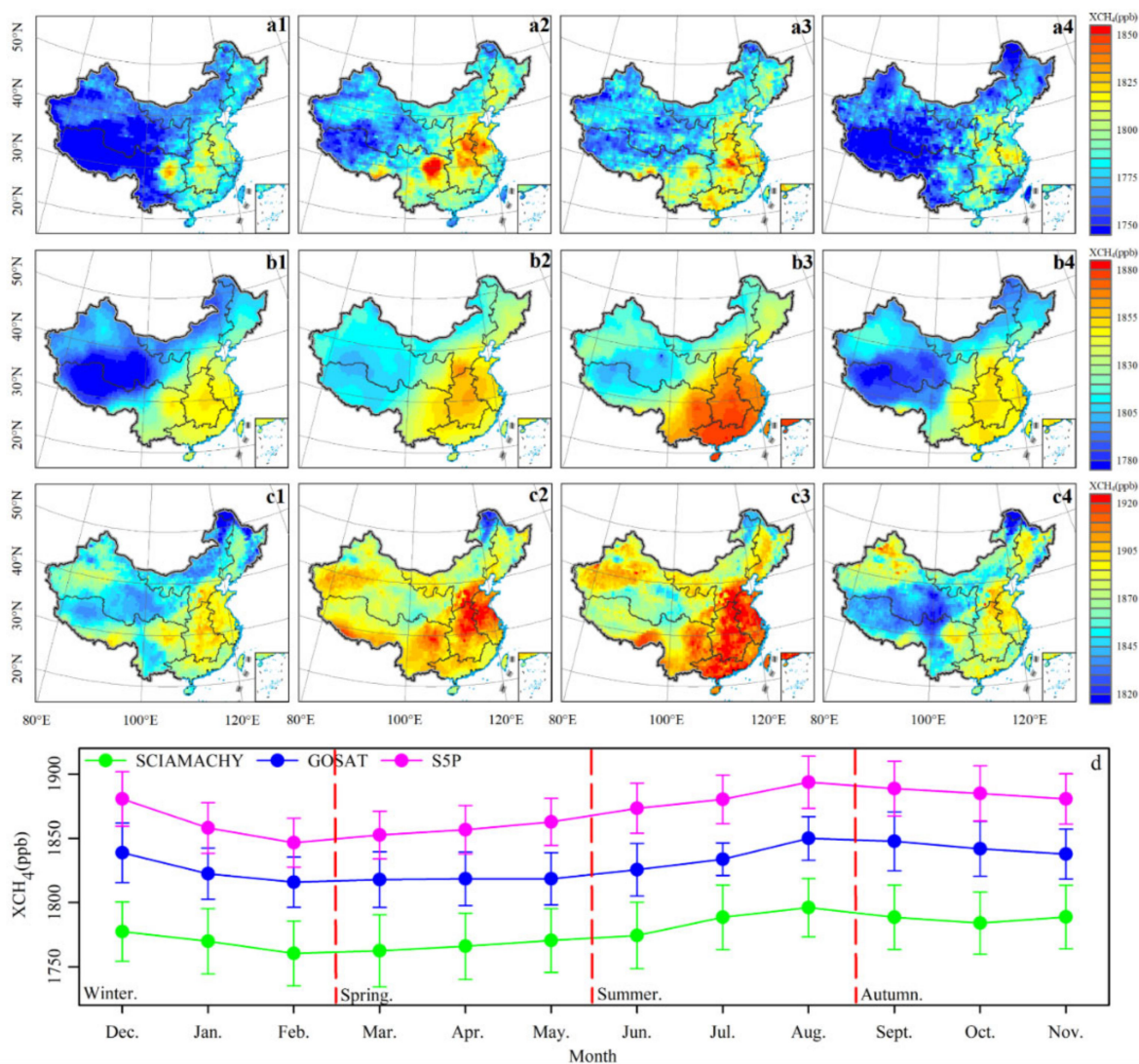


Figure 7. Spatial distributions of the seasonal averages of XCH₄ concentrations across China in the four seasons from SCIAMACHY (2003–2010), GOSAT (2011–2018), and S5P (2019–2021). (a1–a4) Spring, summer, autumn, and winter data from SCIAMACHY; (b1–b4) spring, summer, autumn, and winter data from GOSAT; (c1–c4) spring, summer, autumn, and winter data from S5P; (d) monthly variations of XCH₄ concentrations over China.

3.4. Influence of Rice Paddy on Atmospheric XCH₄ across China

Atmospheric CH₄ mainly come from natural ecology and human activities. CH₄ emissions caused by human activities is considered the dominant contributor, with CH₄ emissions from rice cultivation playing an important role in anthropogenic CH₄ emissions [67]. As one of the most populous countries, China’s rice planting area accounts for about 20% of the world’s total. Moreover, 90% of the rice fields is fully irrigated, which makes CH₄ emissions more frequent [68,69]. Studies have shown that CH₄ emissions from rice in China account for about 29% of the global paddy field emissions [69]. Therefore, it is essential to explore the effect of rice paddies in the spatial distribution and seasonal cycle of atmospheric XCH₄ observed by satellite over China.

Analysis of the spatial distribution consistency between rice paddies and XCH₄ concentrations is illustrated in Figure 8. China’s rice growing areas are mainly distributed in the Southeast, and the hotspots of XCH₄ concentrations were linked to the distribution of areas of rice paddies. Over the last two decades, the average XCH₄ concentration in areas in China with rice paddies was about 1820 ppb, while the average XCH₄ concentration in

areas without rice paddy cover was about 1799 ppb. We further divided the rice planting areas into seven grades [65]. As rice planting density increased in China, the concentration of XCH₄ also increased. In areas where the proportion of rice paddy was less than 0.5%, the average XCH₄ concentration was 1802 ppb. In areas where the proportion of rice paddy was larger than 40%, the average XCH₄ was 1840 ppb (Figure 8b).

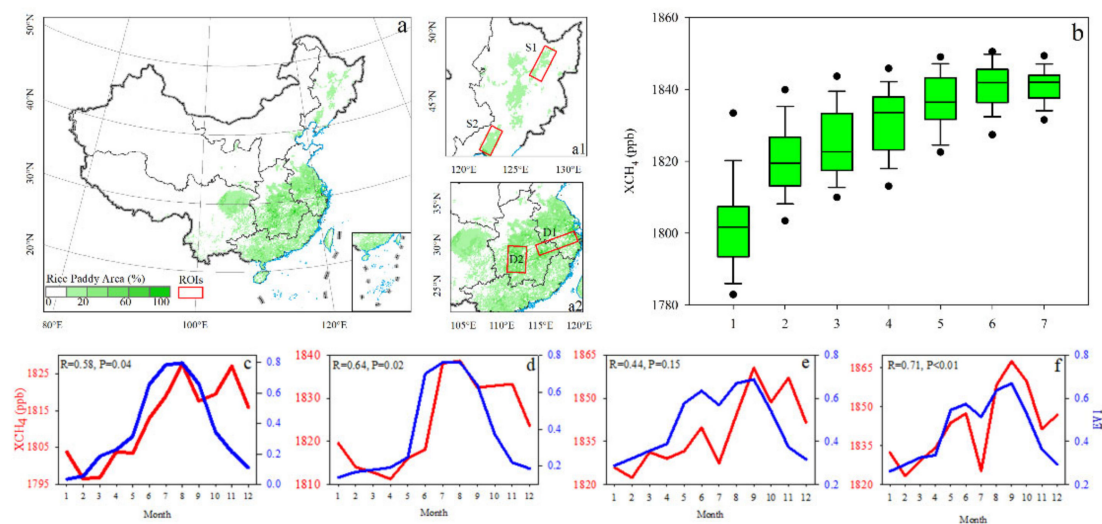


Figure 8. Relationship between rice paddies and XCH₄ concentrations. (a) Spatial distribution of rice paddy areas in China and the four regions of interest (ROIs); (a1) Single cropping rice S1 and S2; (a2) Double cropping of rice D1 and D2; (b) XCH₄ concentrations at seven areas with different proportions of rice paddies (1–7 correspond to <0.5%, 0.5–1%, 1–5%, 5–10%, 10–20%, 20–40%, and >40%, respectively); (c–f) The monthly average of XCH₄ concentrations and enhanced vegetation index (EVI) on rice paddy pixels (rice area >10%) in four regions of interest (ROIs) of S1, S2, D1, and D2, respectively.

We then analyzed the seasonal cycle consistency of paddy rice growth and XCH₄ concentrations. The EVI from MODIS was used to indicate rice plant growth and explore and quantify the seasonal relationship between the growth of paddy rice and XCH₄ concentrations. We selected four typical high-density rice planting areas in China with different cropping systems to explore the seasonal variations of XCH₄ concentrations and rice growth (Figure 8c–f). The seasonal variations of XCH₄ had one peak per year in two regions in Northeast China and two peaks in two regions in Southeast China. The time consistency between XCH₄ and EVI peak indicated the influence of rice growth on XCH₄ concentrations. A single cropping system is used on the Sanjiang Plain in Northeast China, where both XCH₄ and EVI had a single peak between July and September with correlation coefficients of 0.58 and 0.64, respectively (Figure 8c,d). The middle-lower Yangtze Plain in Southeast China is mainly planted with double cropping rice, and there are three crops a year in some areas. Here, there were two peaks around June and September, and the correlation coefficients were 0.44 and 0.71, respectively. Further, we computed the seasonal correlation between XCH₄ and EVI on each paddy's grid (rice density greater than 0.1) to analyze the spatial distribution pattern of seasonal consistency of rice growth and EVI (Figure A5). XCH₄ concentrations and EVI showed a significant positive correlation in the rice planting areas, thereby proving the strong relationship between paddy growth and XCH₄. Regions in China dominated by single rice crops, such as Sichuan Basin, central China, and Liaohe Plain, had high statistically significant positive correlation coefficients. On the Yangtze River delta plain in East China, double cropping rice is more common, with mixed crops during the rotation period and a low Pearson coefficient. This could be affected by the different rice planting times, which lead to more complicated seasonal variations.

4. Conclusions

Satellite observation is a powerful way to study atmospheric methane concentration, but the lifecycle of a single satellite limits long-term study. Based on the XCH₄ product from three satellites (SCIAMACHY, GOSAT, and S5P), we analyzed spatiotemporal variations of atmospheric CH₄ in China during 2003–2021 while accounting for the impact of variability of emission sources. The observations from SCIAMACHY, GOSAT, and S5P satellites in China were highly consistent ($r = 0.72, 0.73, p < 0.01$), and all three XCH₄ data sources showed good agreement with ground measurements.

The XCH₄ concentrations in China generally showed great spatial variation with high values in the east and low values in the west. This was due to different regional CH₄ emission sources, with industrial-related emissions dominant in the north and agricultural emissions dominant in the south. XCH₄ concentrations over China increased significantly from 2003 to 2021, with the trends being stable from 2003 to 2006 and then increasing until 2021. The XCH₄ concentrations showed obvious seasonal cycles in China, with higher values in summer than in winter. This seasonal change was highly correlated with the rice growth cycle.

These findings are helpful for predicting possible feedback due to global warming and scientifically formulating emission reduction strategies. XCH₄ is the comprehensive result of methane emissions, absorption, transportation, and mixing in the atmosphere and is not fully equivalent to methane emissions. Therefore, further research is required to specifically identify the estimation of methane emissions from XCH₄.

Author Contributions: Conceptualization, J.Q. and X.Z.; methodology, J.Q. and X.Z.; software, J.Q., X.Z., L.Z. and M.C.; visualization, X.L.; writing—original draft, J.Q. and X.Z.; writing—review and editing, M.C. and X.L. All authors have read and agreed to the published version of the manuscript.

Funding: This work was supported by the Basic Research Program of Jiangsu Province (NO.: BK20211156).

Data Availability Statement: The relevant data in the paper can be found in the following links. The SCIAMACHY XCH₄ concentration data were provided by Bremen University in Germany (https://www.iup.uni-bremen.de/sciamachy/NIR_NADIR_WFM_DOAS/products/) (accessed on 5 June 2022), the GOSAT XCH₄ concentration data were obtained from the GOSAT project website (<https://www.gosat.nies.go.jp/en/index.html>) (accessed on 5 June 2022), the S5P XCH₄ concentration data were obtained from the National Aeronautics and Space Administration (<https://disc.gsfc.nasa.gov/>) (accessed on 5 June 2022), the ground observations of CH₄ concentrations were from the World Data Centre for Greenhouse Gases (WDCGG) (<https://gaw.kishou.go.jp/>) (accessed on 6 June 2022), the gridded CH₄ emissions across China were from the Emissions Database for Global Atmospheric Research (EDGAR) (http://edgar.jrc.ec.europa.eu/archived_datasets.phpghg) (accessed on 6 June 2022), the enhanced vegetation index (EVI) in China were accessed from the National Aeronautics and Space Administration (<https://modis.gsfc.nasa.gov/data/dataproduct/>) (accessed on 27 June 2022), and the rice harvested area were from EARTHSTAT (<http://www.earthstat.org/>) (accessed on 27 June 2022).

Conflicts of Interest: The authors report no potential conflict of interest.

Appendix A

Table A1. Observed greenhouse gas information by WDCGG station.

Station Name	Longitude (°)	Latitude (°)	Elevation (m)	Time in This Study
AMY	36.54	126.33	42	January 2003–December 2020
LLN	23.47	120.87	2862	August 2006–December 2020
PDI	21.57	103.52	1466	January 2014–November 2020
SDZ	40.65	117.12	287	September 2009–September 2015
UUM	44.44	111.09	992	January 2003–October 2020
WLG	36.29	100.90	3810	January 2003–December 2020

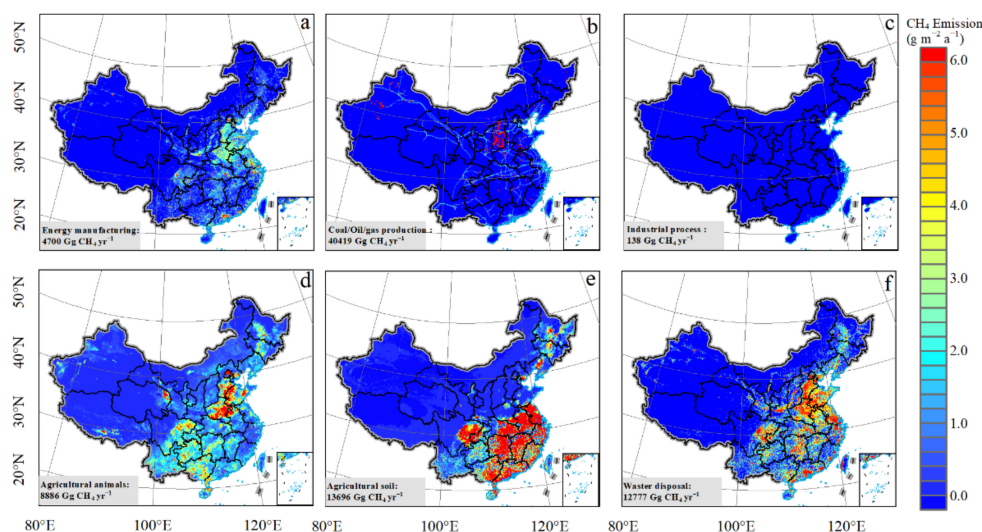


Figure A1. Spatial distribution of the annual mean of CH₄ emission of six categories from EDGAR over China during 2003–2018 ($\text{g m}^{-2} \text{a}^{-1}$). (a) Energy manufacturing (including public electricity and heat production, petroleum refining, manufacture of solid fuels and other energy industries, mobile, solid fuel transformation, distribution of oil products, natural gas, iron and steel production, manufacturing industries and construction (ISIC), civil aviation, road transportation, railways, other transportation, navigation, and other sectors); (b) coal/oil/gas production (including coal mining, oil exploration, oil production, oil transport, oil refining/storage, venting, and flaring); (c) industrial process (including chemical industry, iron and steel production, and ferroalloys production); (d) agricultural animal (including enteric fermentation and manure management); (e) agricultural soil (including rice cultivation, agricultural soils, and field burning of agricultural residues); (f) waste disposal (including solid waste disposal on land, waste incineration, and wastewater handling).

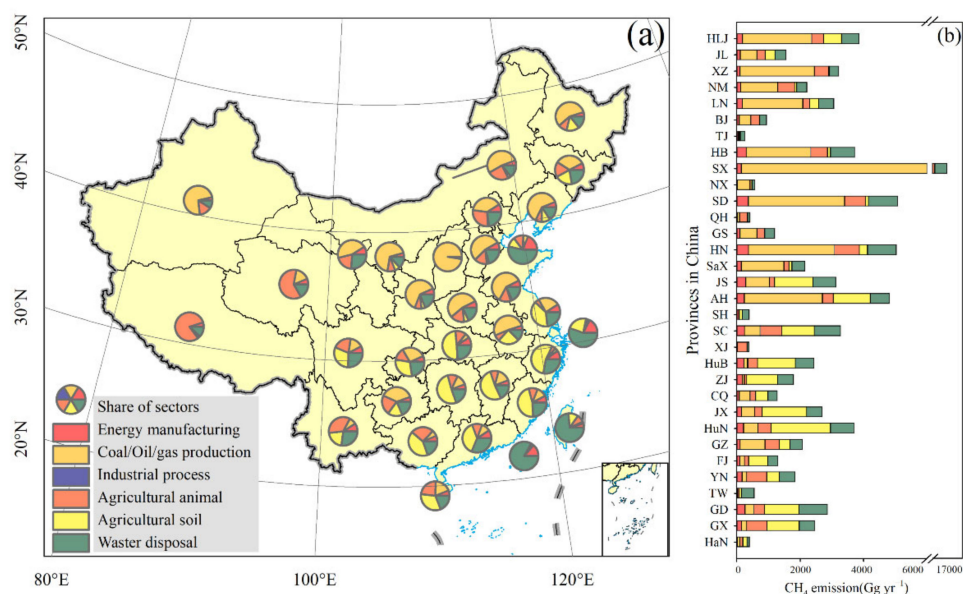


Figure A2. The share of individual sectors in the production of methane emission from EDGAR over China. (a) Spatial distribution of the share of individual sectors in the production of methane emission; (b) The share of individual sectors in the production of methane emission at provincial Scale. The abbreviations of provinces are as follows: BJ, Beijing; TJ, Tianjin; SH, Shanghai; CQ, Chongqing; HB, Heibei Province; HuB, Hubei Province; HN, Henan Province; HuN, Hunan Province; HaN, Hainan Province; SX, Shanxi Province; SaX, Shaanxi Province; GZ, Guizhou Province; XZ, Tibet Autonomous

Region; NX, Ningxia Hui Autonomous Region; GX, Guangxi Zhuang Autonomous Region; GD, Guangdong; YN, Yunnan Province; SC, Sichuan Province; XJ, Xinjiang Uygur Autonomous Region; ZJ, Zhejiang Province; JX, Jiangxi Province; JS, Jiangsu Province; AH, Anhui Province; QH, Qinghai Province; SD, Shandong Province; HLJ, Heilongjiang Province; JL, Jilin Province; LN, Liaoning Province; FJ, Fujian; NM, Inner Mongolia Autonomous Region; GS, Gansu Province; GZ, Guizhou Province.

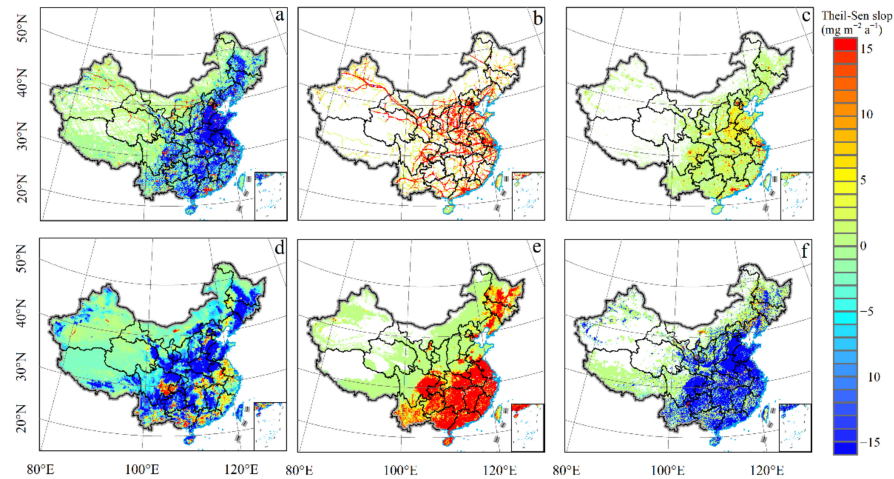


Figure A3. Spatial distribution of the annual rate of increase in methane emission of six categories from EDGAR over China during 2003–2018 ($\text{mg m}^{-2} \text{a}^{-1}$). (a) Energy manufacturing; (b) coal/oil/gas production; (c) industrial process; (d) agricultural animal (including enteric fermentation and manure management); (e) agricultural soil (including rice cultivation and field burning of agricultural residues); (f) waste disposal.

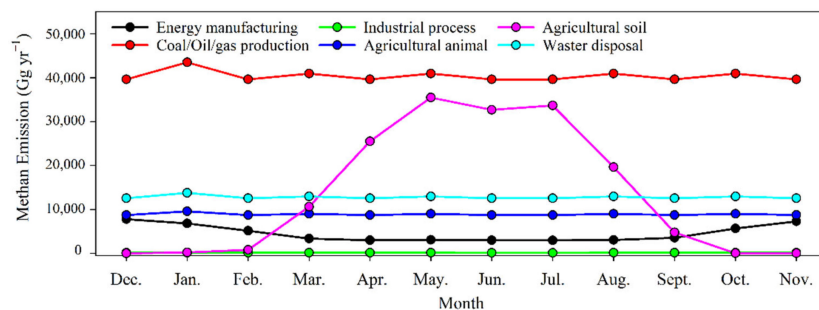


Figure A4. Monthly variations of methane emission of six categories from EDGAR over China.

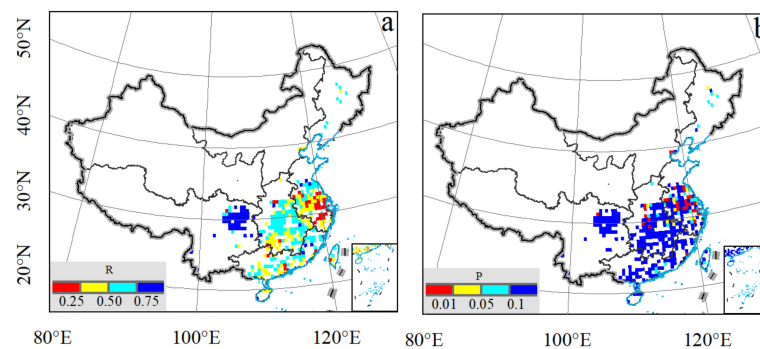


Figure A5. Spatial patterns of correlation coefficients between the seasonal atmospheric methane concentration and rice growth. (a) The spatial distributions of Pearson's correlation coefficients between XCH_4 and EVI; (b) The spatial distributions of significance levels of Pearson's correlation between XCH_4 and EVI.

References

1. Etminan, M.; Myhre, G.; Highwood, E.J.; Shine, K.P. Radiative forcing of carbon dioxide, methane, and nitrous oxide: A significant revision of the methane radiative forcing. *Geophys. Res. Lett.* **2016**, *43*, 12614–12623. [[CrossRef](#)]
2. Canadell, J.G.; Monteiro, P.M.S.; Costa, M.H.; Cunha, L.C.D.; Cox, P.M.; Eliseev, A.V.; Henson, S.; Ishii, M.; Jaccard, S.; Koven, C.; et al. Global Carbon and other Biogeochemical Cycles and Feedbacks. In *Climate Change 2021: The Physical Science Basis. Contribution of Working Group I to the Sixth Assessment Report of the Intergovernmental Panel on Climate Change*; In Press; Masson-Delmotte, V., Zhai, P., Pirani, A., Connors, S.L., Péan, C., Berger, S., Caud, N., Chen, Y., Goldfarb, L., Gomis, M.I., et al., Eds.; Cambridge University Press: Cambridge, UK, 2021.
3. Nisbet, E.G.; Dlugokencky, E.J.; Bousquet, P. Methane on the Rise—Again. *Science* **2014**, *343*, 493–495. [[CrossRef](#)] [[PubMed](#)]
4. Solarin, S.A.; Gil-Alana, L.A. Persistence of Methane Emission in OECD Countries for 1750–2014: A Fractional Integration Approach. *Environ. Model. Assess.* **2021**, *26*, 497–509. [[CrossRef](#)]
5. Zhang, X.Y.; Jiang, H.; Lu, X.H.; Cheng, M.M.; Zhang, X.M.; Li, X.H.; Zhang, L.J. Estimate of methane release from temperate natural wetlands using ENVISAT/SCIAMACHY data in China. *Atmos. Environ.* **2013**, *69*, 191–197. [[CrossRef](#)]
6. Zhang, G.J.; Le, Q. Analysis distribution of CH₄ column concentration using SCIAMACHY data in China. *Geospat. Inf.* **2011**, *9*, 115–117.
7. Kavitha, M.; Nair, P.R. SCIAMACHY observed changes in the column mixing ratio of methane over the Indian region and a comparison with global scenario. *Atmos. Environ.* **2017**, *166*, 454–466. [[CrossRef](#)]
8. Qin, X.C.; Lei, L.P.; He, Z.H.; Zeng, Z.C.; Kawasaki, M.; Ohashi, M.; Matsumi, Y. Preliminary Assessment of Methane Concentration Variation Observed by GOSAT in China. *Adv. Meteorol.* **2015**, *2015*, 125059. [[CrossRef](#)]
9. Kivimäki, E.; Lindqvist, H.; Hakkarainen, J.; Laine, M.; Sussmann, R.; Tsuruta, A.; Detmers, R.; Deutscher, N.M.; Dlugokencky, E.J.; Hase, F.; et al. Evaluation and Analysis of the Seasonal Cycle and Variability of the Trend from GOSAT Methane Retrievals. *Remote Sens.* **2019**, *11*, 882. [[CrossRef](#)]
10. Islam, S.M.N.; Jackson, P.L.; Sweeney, C.; McKain, K.; Frankenberg, C.; Aben, I.; Parker, R.J.; Boesch, H.; Wunch, D. Methane Growth Rate Estimation and Its Causes in Western Canada Using Satellite Observations. *J. Geophys. Res. Atmos.* **2021**, *126*, e2020JD033948. [[CrossRef](#)]
11. Zhang, J.X.; Han, G.; Mao, H.Q.; Pei, Z.P.; Ma, X.; Jia, W.J.; Gong, W. The Spatial and Temporal Distribution Patterns of XCH₄ in China: New Observations from TROPOMI. *Atmosphere* **2022**, *13*, 177. [[CrossRef](#)]
12. Zou, M.M.; Xiong, X.Z.; Saitoh, N.; Warner, J.; Zhang, Y.; Chen, L.F.; Weng, F.Z.; Fan, M. Satellite observation of atmospheric methane: Intercomparison between AIRS and GOSAT TANSO-FTS retrievals. *Atmos. Meas. Tech.* **2016**, *9*, 3567–3576. [[CrossRef](#)]
13. Hu, H.; Landgraf, J.; Detmers, R.; Borsdorff, T.; de Brugh, J.A.; Aben, I.; Butz, A.; Hasekamp, O. Toward Global Mapping of Methane With TROPOMI: First Results and Intersatellite Comparison to GOSAT. *Geophys. Res. Lett.* **2018**, *45*, 3682–3689. [[CrossRef](#)]
14. Zhang, L.J.; Wei, C.; Liu, H.; Jiang, H.; Lu, X.H.; Zhang, X.Y.; Jiang, C. Comparison analysis of global methane concentration derived from SCIAMACHY, AIRS, and GOSAT with surface station measurements. *Int. J. Remote Sens.* **2021**, *42*, 1823–1840. [[CrossRef](#)]
15. Bovensmann, H.; Burrows, J.P.; Buchwitz, M.; Frerick, J.; Noel, S.; Rozanov, V.V.; Chance, K.V.; Goede, A. SCIAMACHY: Mission objectives and measurement modes. *J. Atmos. Sci.* **1999**, *56*, 127–150. [[CrossRef](#)]
16. Buchwitz, M.; de Beek, R.; Burrows, J.P.; Bovensmann, H.; Warneke, T.; Notholt, J.; Meirink, J.F.; Goede, A.; Bergamaschi, P.; Korner, S.; et al. Atmospheric methane and carbon dioxide from SCIAMACHY satellite data: Initial comparison with chemistry and transport models. *Atmos. Chem. Phys.* **2005**, *5*, 941–962. [[CrossRef](#)]
17. Barkley, M.P.; Monks, P.S.; Engelen, R.J. Comparison of SCIAMACHY and AIRS CO₂ measurements over North America during the summer and autumn of 2003. *Geophys. Res. Lett.* **2006**, *33*, L20805. [[CrossRef](#)]
18. Buchwitz, M.; Rozanov, V.V.; Burrows, J.P. A near-infrared optimized DOAS method for the fast global retrieval of atmospheric CH₄, CO, CO₂, H₂O, and N₂O total column amounts from SCIAMACHY Envisat-1 nadir radiances. *J. Geophys. Res. Atmos.* **2000**, *105*, 15231–15245. [[CrossRef](#)]
19. Burrows, J.P.; Holzle, E.; Goede, A.; Visser, H.; Fricke, W. SCIAMACHY—scanning imaging absorption spectrometer for atmospheric cartography. *Acta Astronaut.* **1995**, *35*, 445–451. [[CrossRef](#)]
20. Kuze, A.; Suto, H.; Nakajima, M.; Hamazaki, T. Thermal and near infrared sensor for carbon observation Fourier-transform spectrometer on the Greenhouse Gases Observing Satellite for greenhouse gases monitoring. *Appl. Opt.* **2009**, *48*, 6716–6733. [[CrossRef](#)]
21. Morino, I.; Uchino, O.; Inoue, M.; Yoshida, Y.; Yokota, T.; Wennberg, P.O.; Toon, G.C.; Wunch, D.; Roehl, C.M.; Notholt, J.; et al. Preliminary validation of column-averaged volume mixing ratios of carbon dioxide and methane retrieved from GOSAT short-wavelength infrared spectra. *Atmos. Meas. Tech.* **2011**, *4*, 1061–1076. [[CrossRef](#)]
22. Suto, H.; Kataoka, F.; Kikuchi, N.; Knuteson, R.O.; Butz, A.; Haun, M.; Buijs, H.; Shiomi, K.; Imai, H.; Kuze, A. Thermal and near-infrared sensor for carbon observation Fourier transform spectrometer-2 (TANSO-FTS-2) on the Greenhouse gases Observing SATellite-2 (GOSAT-2) during its first year in orbit. *Atmos. Meas. Tech.* **2021**, *14*, 2013–2039. [[CrossRef](#)]
23. Dlugokencky, E.J.; Steele, L.P.; Lang, P.M.; Masarie, K.A. The growth rate and distribution of atmospheric methane. *J. Geophys. Res. Atmos.* **1994**, *99*, 17021–17043. [[CrossRef](#)]

24. Yang, Q.; Guan, L.; Tao, F.; Liang, M.; Sun, W.Q. Changes of CH₄ Concentrations Obtained by Ground-based Observations at Five Atmospheric Background Stations in China. *Environ. Sci. Technol.* **2018**, *41*, 1–7.
25. Huete, A.; Didan, K.; Miura, T.; Rodriguez, E.P.; Gao, X.; Ferreira, L.G. Overview of the radiometric and biophysical performance of the MODIS vegetation indices. *Remote Sens. Environ.* **2002**, *83*, 195–213. [[CrossRef](#)]
26. Xu, J.H.; Li, W.T.; Xie, H.M.; Wang, Y.X.; Wang, L.; Hu, F. Long-Term Trends and Spatiotemporal Variations in Atmospheric XCH₄ over China Utilizing Satellite Observations. *Atmosphere* **2022**, *13*, 525. [[CrossRef](#)]
27. Wu, X.D.; Zhang, X.Y.; Chuai, X.W.; Huang, X.J.; Wang, Z. Long-Term Trends of Atmospheric CH₄ Concentration across China from 2002 to 2016. *Remote Sens.* **2019**, *11*, 538. [[CrossRef](#)]
28. Weatherhead, E.C.; Reinsel, G.C.; Tiao, G.C.; Meng, X.L.; Choi, D.S.; Cheang, W.K.; Keller, T.; DeLuisi, J.; Wuebbles, D.J.; Kerr, J.B.; et al. Factors affecting the detection of trends: Statistical considerations and applications to environmental data. *J. Geophys. Res. Atmos.* **1998**, *103*, 17149–17161. [[CrossRef](#)]
29. Zhang, X.Y.; Chuai, X.W.; Liu, L.; Zhang, W.T.; Lu, X.H.; Zhao, L.M.; Chen, D.M. Decadal Trends in Wet Sulfur Deposition in China Estimated From OMI SO₂ Columns. *J. Geophys. Res. Atmos.* **2018**, *123*, 10796–10811. [[CrossRef](#)]
30. Hamed, K.H.; Rao, A.R. A modified Mann-Kendall trend test for autocorrelated data. *J. Hydrol.* **1998**, *204*, 182–196. [[CrossRef](#)]
31. Wang, J.J.; Zhang, Y.N.; Sun, X.Y. Trend of Light Rain Precipitation Days of Hangzhou in Recent 60 Years. *Bull. Sci. Technol.* **2019**, *35*, 41–45. [[CrossRef](#)]
32. Gocic, M.; Trajkovic, S. Analysis of changes in meteorological variables using Mann-Kendall and Sen's slope estimator statistical tests in Serbia. *Global Planet. Chang.* **2013**, *100*, 172–182. [[CrossRef](#)]
33. Aziz, O.; Burn, D.H. Trends and variability in the hydrological regime of the Mackenzie River Basin. *J. Hydrol.* **2006**, *319*, 282–294. [[CrossRef](#)]
34. Cannarozzo, M.; Noto, L.V.; Viola, F. Spatial distribution of rainfall trends in Sicily (1921–2000). *Phys. Chem. Earth* **2006**, *31*, 1201–1211. [[CrossRef](#)]
35. Wilks, D.S. On “Field Significance” and the False Discovery Rate. *J. Appl. Meteorol. Clim.* **2006**, *45*, 1181–1189. [[CrossRef](#)]
36. Xu, Y.Y.; Wang, J.L.; Sun, J.L.; Xu, Y.; Harris, W. Spatial and Temporal Variations of Lower Tropospheric Methane During 2010–2011 in China. *IEEE J. Stars* **2012**, *5*, 1464–1473. [[CrossRef](#)]
37. Zhang, X.M.; Zhang, X.Y.; Zhang, L.J.; Li, X.H. Accuracy Comparison of Monthly AIRS, GOSAT and SCIAMACHY Data in Monitoring Atmospheric CH₄ Concentration. In Proceedings of the 21st International Conference on Geoinformatics, Kaifeng, China, 20–22 June 2013.
38. Saito, R.; Patra, P.K.; Sweeney, C.; Machida, T.; Krol, M.; Houweling, S.; Bousquet, P.; Agusti-Panareda, A.; Belikov, D.; Bergmann, D.; et al. TransCom model simulations of methane: Comparison of vertical profiles with aircraft measurements. *J. Geophys. Res. Atmos.* **2013**, *118*, 3891–3904. [[CrossRef](#)]
39. Kulawik, S.S.; Worden, J.R.; Payne, V.H.; Fu, D.J.; Wofsy, S.C.; McKain, K.; Sweeney, C.; Daube, B.C.; Lipton, A.; Polonsky, I.; et al. Evaluation of single-footprint AIRS CH₄ profile retrieval uncertainties using aircraft profile measurements. *Atmos. Meas. Tech.* **2021**, *14*, 335–354. [[CrossRef](#)]
40. Lorente, A.; Borsdorff, T.; Butz, A.; Hasekamp, O.; Aan De Brugh, J.; Schneider, A.; Wu, L.H.; Hase, F.; Kivi, R.; Wunch, D.; et al. Methane retrieved from TROPOMI: Improvement of the data product and validation of the first 2 years of measurements. *Atmos Meas Tech.* **2021**, *14*, 665–684. [[CrossRef](#)]
41. Xiong, X.Z.; Barnett, C.; Maddy, E.; Sweeney, C.; Liu, X.P.; Zhou, L.H.; Goldberg, M. Characterization and validation of methane products from the Atmospheric Infrared Sounder (AIRS). *J. Geophys. Res. Biogeo.* **2008**, *113*, 500. [[CrossRef](#)]
42. Schneising, O.; Bergamaschi, P.; Bovensmann, H.; Buchwitz, M.; Burrows, J.P.; Deutscher, N.M.; Griffith, D.; Heymann, J.; Macatangay, R.; Messerschmidt, J.; et al. Atmospheric greenhouse gases retrieved from SCIAMACHY: Comparison to ground-based FTS measurements and model results. *Atmos. Chem. Phys.* **2012**, *12*, 1527–1540. [[CrossRef](#)]
43. Dils, B.; De Maziere, M.; Muller, J.F.; Blumenstock, T.; Buchwitz, M.; de Beek, R.; Demoulin, P.; Duchatelet, P.; Fast, H.; Frankenberg, C.; et al. Comparisons between SCIAMACHY and ground-based FTIR data for total columns of CO, CH₄, CO₂ and N₂O. *Atmos. Chem. Phys.* **2006**, *6*, 1953–1976. [[CrossRef](#)]
44. Gloudemans, A.; Schrijver, H.; Hasekamp, O.P.; Aben, I. Error analysis for CO and CH₄ total column retrievals from SCIAMACHY 2.3 μ m spectra. *Atmos. Chem. Phys.* **2008**, *8*, 3999–4017. [[CrossRef](#)]
45. Dan-dan, L.; Yin-bo, H.; Zhen-song, C.; Xing-ji, L.U.; Yu-song, S.; Qian-si, T.U. Analysis of Total Columns of Greenhouse Gas Based on Direct Observation and Comparison with Satellite Data in Hefei. *Acta Photonica Sin.* **2020**, *49*, 159–168. [[CrossRef](#)]
46. Inoue, M.; Morino, I.; Uchino, O.; Miyamoto, Y.; Saeki, T.; Yoshida, Y.; Yokota, T.; Sweeney, C.; Tans, P.P.; Biraud, S.C.; et al. Validation of XCH₄ derived from SWIR spectra of GOSAT TANSO-FTS with aircraft measurement data. *Atmos. Meas. Tech.* **2014**, *7*, 2987–3005. [[CrossRef](#)]
47. Mermigkas, M.; Topaloglou, C.; Balis, D.; Koukouli, M.E.; Hase, F.; Dubravica, D.; Borsdorff, T.; Lorente, A. FTIR Measurements of Greenhouse Gases over Thessaloniki, Greece in the Framework of COCCON and Comparison with S5P/TROPOMI Observations. *Remote Sens.* **2021**, *13*, 3395. [[CrossRef](#)]
48. Sha, M.K.; Langerock, B.; Blavier, J.; Blumenstock, T.; Borsdorff, T.; Buschmann, M.; Dehn, A.; De Maziere, M.; Deutscher, N.M.; Feist, D.G.; et al. Validation of methane and carbon monoxide from Sentinel-5 Precursor using TCCON and NDACC-IRWG stations. *Atmos. Meas. Tech.* **2021**, *14*, 6249–6304. [[CrossRef](#)]

49. Tu, Q.S.; Hase, F.; Blumenstock, T.; Kivi, R.; Heikkinen, P.; Sha, M.K.; Raffalski, U.; Landgraf, J.; Lorente, A.; Borsdorff, T.; et al. Intercomparison of atmospheric CO₂ and CH₄ abundances on regional scales in boreal areas using Copernicus Atmosphere Monitoring Service (CAMS) analysis, COllaborative Carbon Column Observing Network (COCCON) spectrometers, and Sentinel-5 Precursor satellite observations. *Atmos. Meas. Tech.* **2020**, *13*, 4751–4771. [[CrossRef](#)]
50. Monteil, G.; Houweling, S.; Butz, A.; Guerlet, S.; Schepers, D.; Hasekamp, O.; Frankenberg, C.; Scheepmaker, R.; Aben, I.; Rockmann, T. Comparison of CH₄ inversions based on 15 months of GOSAT and SCIAMACHY observations. *J. Geophys. Res. Atmos.* **2013**, *118*, 11807–11823. [[CrossRef](#)]
51. Etheridge, D.M.; Pearman, G.I.; Fraser, P.J. Changes in Tropospheric Methane Between 1841 and 1978 from a High Accumulation-Rate Antarctic Ice Core. *Tellus B* **1992**, *44*, 282–294. [[CrossRef](#)]
52. Brenninkmeijer, C.; Crutzen, P.; Boumard, F.; Dauer, T.; Dix, B.; Ebinghaus, R.; Filippi, D.; Fischer, H.; Franke, H.; Friess, U.; et al. Civil Aircraft for the regular investigation of the atmosphere based on an instrumented container: The new CARIBIC system. *Atmos. Chem. Phys.* **2007**, *7*, 4953–4976. [[CrossRef](#)]
53. Schuck, T.J.; Ishijima, K.; Patra, P.K.; Baker, A.K.; Machida, T.; Matsueda, H.; Sawa, Y.; Umezawa, T.; Brenninkmeijer, C.A.M.; Lelieveld, J. Distribution of methane in the tropical upper troposphere measured by CARIBIC and CONTRAIL aircraft. *J. Geophys. Res. Atmos.* **2012**, *117*, D19304. [[CrossRef](#)]
54. Blake, D.R.; Mayer, E.W.; Tyler, S.C.; Makide, Y.; Montague, D.C.; Rowland, F.S. Global Increase In Atmospheric Methane Concentrations Between 1978 and 1980. *Geophys. Res. Lett.* **1982**, *9*, 477–480. [[CrossRef](#)]
55. Cunnold, D.M. In situ measurements of atmospheric methane at GAGE/AGAGE sites during 1985–2000 and resulting source inferences. *J. Geophys. Res.* **2002**, *107*, ACH 20-1–ACH 20-18. [[CrossRef](#)]
56. Dlugokencky, E.J.; Bruhwiler, L.; White, J.W.C.; Emmons, L.K.; Novelli, P.C.; Montzka, S.A.; Masarie, K.A.; Lang, P.M.; Crotwell, A.M.; Miller, J.B.; et al. Observational constraints on recent increases in the atmospheric CH₄ burden. *Geophys. Res. Lett.* **2009**, *36*, L18803. [[CrossRef](#)]
57. Zhou, L.; Worthy, D.; Lang, P.M.; Ernst, M.K.; Zhang, X.C.; Wen, Y.P.; Li, J.L. Ten years of atmospheric methane observations at a high elevation site in Western China. *Atmos. Environ.* **2004**, *38*, 7041–7054. [[CrossRef](#)]
58. Crippa, M.; Solazzo, E.; Huang, G.; Guizzardi, D.; Koffi, E.; Muntean, M.; Schieberle, C.; Friedrich, R.; Janssens-Maenhout, G. High resolution temporal profiles in the Emissions Database for Global Atmospheric Research. *Sci. Data* **2020**, *7*, 121. [[CrossRef](#)]
59. Van Groenigen, K.J.; van Kessel, C.; Hungate, B.A. Increased greenhouse-gas intensity of rice production under future atmospheric conditions. *Nat. Clim. Chang.* **2013**, *3*, 288–291. [[CrossRef](#)]
60. Kirschke, S.; Bousquet, P.; Ciais, P.; Saunois, M.; Canadell, J.G.; Dlugokencky, E.J.; Bergamaschi, P.; Bergmann, D.; Blake, D.R.; Bruhwiler, L.; et al. Three decades of global methane sources and sinks. *Nat. Geosci.* **2013**, *6*, 813–823. [[CrossRef](#)]
61. Saunois, M.; Stavert, A.R.; Poulter, B.; Bousquet, P.; Canadell, J.G.; Jackson, R.B.; Raymond, P.A.; Dlugokencky, E.J.; Houweling, S.; Patra, P.K.; et al. The Global Methane Budget 2000–2017. *Earth Syst. Sci. Data* **2020**, *12*, 1561–1623. [[CrossRef](#)]
62. Zhang, H.H.; Li, C.; Gao, Y.B.; Fang, X.J.; Xiong, W.; Mas, J.J. Research for High-Level OH Radicals Spatio-Temporal Distribution Characteristics and Its Formation Mechanism. *J. Atmos. Environ. Opt.* **2017**, *12*, 292–304. [[CrossRef](#)]
63. Zhang, X.Y.; Bai, W.G.; Zhang, P.; Wang, W.H. Spatiotemporal variations in mid-upper tropospheric methane over China from satellite observations. *Chin. Sci. Bull.* **2011**, *56*, 3321–3327. [[CrossRef](#)]
64. Zhang, D.Y.; Liao, H.; Wang, Y.S. Simulated Spatial Distribution and Seasonal Variation of Atmospheric Methane over China: Contributions from Key Sources. *Adv. Atmos. Sci.* **2014**, *31*, 283–292. [[CrossRef](#)]
65. Zhang, G.L.; Xiao, X.M.; Dong, J.W.; Xin, F.F.; Zhang, Y.; Qin, Y.W.; Doughty, R.B.; Moore, B. Fingerprint of rice paddies in spatial-temporal dynamics of atmospheric methane concentration in monsoon Asia. *Nat. Commun.* **2020**, *11*, 554. [[CrossRef](#)] [[PubMed](#)]
66. Tokida, T.; Adachi, M.; Cheng, W.G.; Nakajima, Y.; Fumoto, T.; Matsushima, M.; Nakamura, H.; Okada, M.; Sameshima, R.; Hasegawa, T. Methane and soil CO₂ production from current-season photosynthates in a rice paddy exposed to elevated CO₂ concentration and soil temperature. *Glob. Chang. Biol.* **2011**, *17*, 3327–3337. [[CrossRef](#)]
67. Tian, H.Q.; Lu, C.Q.; Ciais, P.; Michalak, A.M.; Canadell, J.G.; Saikawa, E.; Huntzinger, D.N.; Gurney, K.R.; Sitch, S.; Zhang, B.W.; et al. The terrestrial biosphere as a net source of greenhouse gases to the atmosphere. *Nature* **2016**, *531*, 225. [[CrossRef](#)]
68. Chen, H.; Zhu, Q.A.; Peng, C.H.; Wu, N.; Wang, Y.F.; Fang, X.Q.; Jiang, H.; Xiang, W.H.; Chang, J.; Deng, X.W.; et al. Methane emissions from rice paddies natural wetlands, lakes in China: Synthesis new estimate. *Glob. Chang. Biol.* **2013**, *19*, 19–32. [[CrossRef](#)]
69. Yan, X.Y.; Akiyama, H.; Yagi, K.; Akimoto, H. Global estimations of the inventory and mitigation potential of methane emissions from rice cultivation conducted using the 2006 Intergovernmental Panel on Climate Change Guidelines. *Glob. Biogeochem. Cy.* **2009**, *23*, GB2002. [[CrossRef](#)]